Journal of
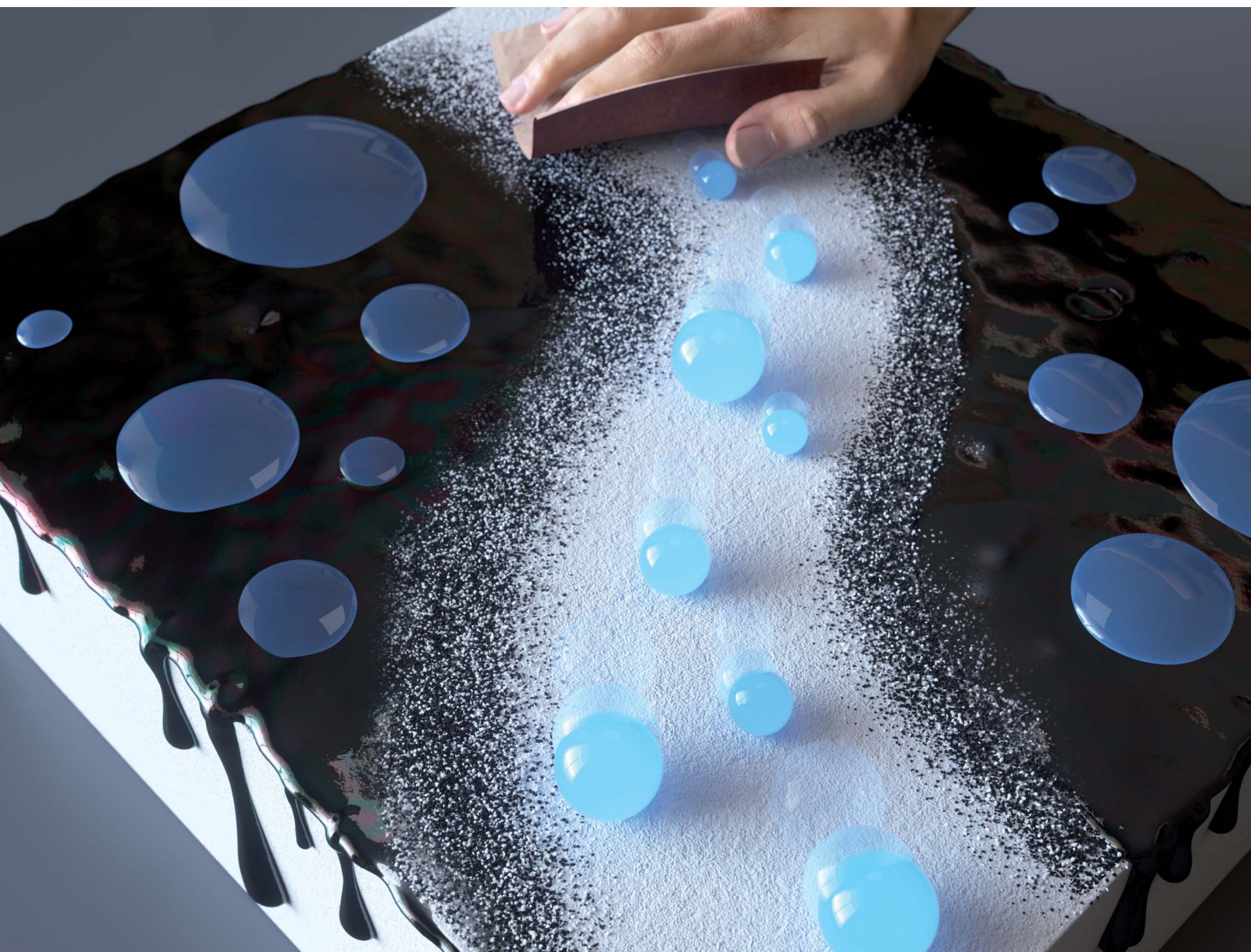# Materials Chemistry A

Materials for energy and sustainability

rsc.li/materials-a

ROYAL SOCIETY
OF **CHEMISTRY**

PAPER
Gi Byoung Hwang *et al.*
Transition from the Wenzel to Cassie–Baxter state by
PFOTES/TiO$_2$ nanoparticles leading to a mechanically robust
and damage/contamination-recoverable surface

Check for updates

Transition from the Wenzel to Cassie–Baxter state by PFOTES/TiO₂ nanoparticles leading to a mechanically robust and damage/contamination-recoverable surface†

Ki Joon Heo, [ID] ‡[ab] Jae Hyun Yoo,‡[c] Juhun Shin, [ID] [a] Wei Huang,[de] Manish K. Tiwari, [ID] [de] Jae Hee Jung, [ID] [f] Ivan P. Parkin, [ID] [a] Claire J. Carmalt [ID] [a] and Gi Byoung Hwang [ID] *[a]

Here, we introduce a highly robust and damage/contamination-recoverable superhydrophobic surface consisting of 1*H*,1*H*,2*H*,2*H*-perfluorooctyltriethoxysilane bonded titanium dioxide nanoparticles (PFOTES/TiO₂ NPs) and ultra-high-molecular-weight polyethylene (UHMWPE). The addition of PFOTES/TiO₂ NPs into UHMWPE transformed the surface wettability from the Wenzel to the Cassie–Baxter state. The superhydrophobicity of the surfaces remained after 80 or 100 cycles of sand dropping, sandpaper abrasion and adhesive tape peeling, and even after making 2000 scalpel scratches. They were stable under heat at 180 °C and repellent to water droplets with various water pH levels. The mechanical compression, impact, and bending tests showed that the mechanical strengths of the superhydrophobic surfaces were more prominent than those of high-strength cement, a highly robust material. Even when the surfaces were damaged and contaminated by a gas flame, aqua regia, paint, oil and blood, their superhydrophobicity was readily recovered through a simple abrasion process by rubbing with sandpaper. This strategy for the production of a robust superhydrophobic surface recoverable from damage and contamination could help move the superhydrophobic surface to real-world applications.

Introduction

Superhydrophobic surfaces have a water contact angle of >150° and a rolling off angle/contact angle hysteresis of <5°, indicating that the surfaces are extremely water-repellent.[1] Over the decades, superhydrophobic surfaces have been studied extensively.[2–17] It has been reported that these surfaces have self-cleaning, anti-biofouling, anti-corrosion and anti-icing/fogging properties and hence hold great potential for various applications.[2–10] The water repellent properties of super-hydrophobic surfaces are attributed to a low surface energy and nano/micro-scale surface roughness, minimising the interaction between the liquid and surface.[18–21]

However, real-world application of superhydrophobic surfaces remains a huge challenge because the hydrophobic nano/microstructures on the surface are typically fragile, and these surfaces are readily contaminated by other fluid types or an organic contaminant, causing a permanent loss of superhydrophobicity.[22–25] Various strategies have been explored to address the problem.[26] Lu *et al.* (2015) employed double-sided tape or an adhesive spray to obtain a robust bonding between superhydrophobic coatings and substrates.[27] This strategy could be applied to various substrates, including paper, cotton, steel and glass, creating a robust superhydrophobic surface. Peng *et al.* (2018) reported an organic nanocomposite coating consisting of fluorinated epoxy resin, perfluoropolyether and fluoropolymeric nanoparticles.[28] It was shown that the coating maintained superhydrophobicity by scarifying the surface's upper layers under various mechanically and chemically harsh conditions. Wang *et al.* (2020) introduced microstructure armour-protected superhydrophobic surface.[29] They proposed a way to prevent wear of the nanostructures by enclosing the water-repellent but mechanically fragile nanostructures in microstructure pockets. Such approaches improve surface robustness, but they are still insufficient for real-world application because, firstly, most of the

ᵃDepartment of Chemistry, University College London, London WC1H 0AJ, UK. E-mail: gi-byoung.hwang.14@ucl.ac.uk

ᵇSchool of Mechanical Engineering, Chonnam National University, Gwangju 61186, Republic of Korea

ᶜLab. M. 0, 47-24, Achasan-ro 15-gil, Seongdong-gu, Seoul 08389, Republic of Korea

ᵈNanoengineered Systems Laboratory, UCL Mechanical Engineering, University College London, London WC1E 7JE, UK

ᵉWellcome/EPSRC Centre for Interventional and Surgical Sciences, University College London, London W1W 7TS, UK

ᶠDepartment of Mechanical Engineering, Sejong University, Seoul 05006, Republic of Korea

‡ These authors contributed equally to this work.

techniques are complicated and time-consuming; secondly, they mainly focus on wear-resistant surfaces; and thirdly, once they are damaged, the surfaces cannot recover their water repellency.[26–30]

Here, we introduce a mechanically robust and damage/contamination recoverable superhydrophobic surface consisting of ultra-high-molecular-weight polyethylene (UHMWPE) and $1H,1H,2H,2H$-perfluorooctyltriethoxysilane bonded titanium dioxide nanoparticles (PFOTES/TiO$_2$ NPs). The surface's microstructures were fabricated by a simple sanding process, and the micro-roughness was easily controlled by changing the grit number of the sandpaper. By adding PFOTES/TiO$_2$ NPs to UHMWPE, the surface's wettability mode was transformed from the Wenzel to the Cassie–Baxter state, resulting in a superhydrophobic surface with a water contact angle of ~160° and a low contact angle hysteresis/rolling-off angle of <5°. The mechanical strengths of the superhydrophobic surfaces were more prominent than those of commercial high-strength cement, and their superhydrophobicity remained after 80 or 100 cycles of sand dropping, sandpaper abrasion and adhesive tape peeling, and even after making 2000 scalpel scratches. In addition, the surfaces readily recovered their superhydrophobicity through a simple sanding process when damaged under extreme conditions.

Experimental section

PFOTES/TiO$_2$ NP synthesis

1 g of $1H,1H,2H,2H$-perfluorooctyltriethoxysilane (Sigma-Aldrich, UK) was mixed with 99.0 g of pure ethanol solution with continuous agitation. 13 g of titanium oxide(IV) nanoparticles with a size of 21 nm (TiO$_2$, Sigma-Aldrich, UK) were added to the solution, which was vortexed for 5 min, and then kept at room temperature for 24 h. The solution was coated onto a glass substrate and aerially dried in a dark room for 3 h, resulting in a superhydrophobic coating. The coating layer was scrubbed off using a spatula and ground with an electric blender.

Production of the superhydrophobic surface

PFOTES/TiO$_2$ NPs and UHMWPE powder were mixed in ratios of 3 : 7, 4 : 6, 5 : 5, and 6 : 4 in an electric blender. 30 g of the mixture was placed into the stainless mould consisting of three parts (Fig. S1†) and thermally pressed at 150 °C for 45 min. The pressure applied on the mixture was about 11 MPa. After that, the solid samples with a thickness of ~1 cm and a diameter of ~6 cm were collected and cooled down to room temperature. To control the surface roughness, the sample was placed on sandpaper, and then under a load pressure ranging from 46 to 68 kPa, the sample was moved back and forth for 15 cm along a ruler. 100 cycles were performed to be sure that the surface was uniformly worn. Grit no. 120, 240, 400, 800, and 1200 were used for the sanding process.

X-ray photoelectron spectroscopy (XPS), attenuated total reflectance-infrared spectroscopy (ATR-IR) and scanning electron microscopy (SEM)

XPS and ATR-IR spectrum analyses were performed to characterise the NPs; a ThermoScientific XPS (UK) with a monochromatic Al Kα X-ray source (1486.96 eV) and Bruker Tensor 27 FTIR spectrometer were used to obtain the XPS and IR data. SEM (JEOL Inc., UK) analysis was performed to investigate the microstructures on the sample's surface. Gold coatings were deposited on the samples through a 60 s sputter coating to prevent surface charging. The images of the samples were taken at an accelerating voltage of 5 kV. Field Emission (FE)-SEM analysis was performed to investigate the nanostructures on the microstructures. A platinum coating was deposited on the sample through 180 s sputter coating to prevent surface charging. The images of the samples were taken at an accelerating voltage of 15 kV.

The measurement of water contact angle, rolling off-angle, and contact angle hysteresis

The water contact angle, rolling off-angle and contact angle hysteresis of the sample were measured using a contact angle meter (First Ten Angstroms, Inc., USA). A droplet (10 μL) of DI water was placed onto the sample surface, and the image was taken side-on. The images were analysed using ImageJ software. The rolling off-angle was measured at tilted angles of 1°–90°. The contact angle hysteresis was calculated as the difference of the advancing angle and receding angle.[31]

Stylus profilometry and atomic force microscopy

The surface roughness of the sample was measured using the stylus profiler (DektakXT, Bruker Corporation, UK). The stylus profiler was employed to measure the roughness of microstructures on the sample. A stylus tip with a radius of 5 μm was used. An area of 500 μm × 500 μm on the sample was measured in each measurement.

Conventional robustness test

Conventional stability tests were employed to investigate the surface robustness, including sandpaper abrasion, sand grain dropping, adhesive tape peeling, and knife scratching. For the tests, superhydrophobic surfaces containing 40, 50, and 60% PFOTES/TiO$_2$ NPs with dimensions of 2 cm × 2 cm were used. The tape peeling test was conducted using a new piece of Sellotape each time. At each time, a 250 g weight was loaded and rubbed on the surface after the tape attachment. For the sand dropping test, 80 g of coarse sand grains, which are 1–2 mm in length, was dropped from a height of 30 cm. For the sandpaper abrasion test, the superhydrophobic surface was placed face down on Grit no. 80 sandpaper and a 250 g weight was loaded onto the superhydrophobic surface. The load pressure on the surface was about 6.1 kPa. The surface moved back and forth for 15 cm along a plastic ruler. The scalpel scratch tests were performed by scratching the superhydrophobic surfaces up to 2000 times with the tip of a scalpel blade, which is exceptionally sharp.

Compressive strength measurement

The samples' compressive strengths were measured using a universal testing machine (model 5969, 50 kN load cell, Instron, UK) at a loading rate of 5 mm min^{-1}. Uniformly sized

This journal is © The Royal Society of Chemistry 2024

J. Mater. Chem. A, 2024, **12**, 3886–3895 | **3887**

cubic samples (1 cm × 1 cm × 1 cm) were prepared for the experiment. An acquisition system recorded peak loads during the test.

Bending strength measurement

Cuboid samples (5 cm × 0.8 cm × 0.8 cm) were prepared for the bending tests. A three-point bending test was performed using the universal testing machine at room temperature. The load was applied at a constant cross-head speed of 5 mm min^{-1}. An acquisition system recorded peak loads during the test.

Impact test using an iron ball

The impact test was performed using an iron ball with a diameter of 3 cm and a weight of 265 g. For the experiment, samples with a thickness of 0.8 cm were prepared. The iron ball was vertically impacted onto the centre of the sample at a distance of 5 to 100 cm. The impact energy was calculated at the fracture point of the sample.

Repellent test against water droplets with pH 1–13

The water contact angle, rolling off-angle and contact angle hysteresis of superhydrophobic surfaces containing 40, 50, and 60% PFOTES/TiO$_2$ NPs were measured using water droplets with pH 1–13. For pH control, sodium hydroxide (NaOH), hydrochloric acid (HCl), and a pH meter were used. HCl and NaOH were mixed with DI water for <pH 7 and >pH 7, respectively.

Surface damage/contamination and recovery

A blue gas flame with a temperature of ~2000 °C was used to burn the superhydrophobic surface. The surface was exposed to the flame until the surface colour changed from white to black. For the surface corrosion, aqua regia was prepared by mixing nitric acid (HNO$_3$, Sigma-Aldrich) and hydrochloric acid (HCl, Sigma-Aldrich) in the molecular ratio of 3 : 1. The superhydrophobic surface was immersed in the solution for 1 h. Then, it was collected and washed using DI water. For surface contamination, paint and silicone oil were used. The paint was coated on the superhydrophobic surface using a paint roller and dried for 24 h. Another surface was dipped in silicone oil for 5 s to make the surface wet by the oil and then collected. The excessive oil on the surface was removed using a paper wipe. The water contact angles of the damaged and contaminated surfaces were measured using a contact angle meter.

To recover the water repellent properties, the contaminated or damaged surface was placed face down on Grit no. 120 sandpaper, and then the surface moved back and forth for 15 cm along a plastic ruler under a load pressure ranging from 46 to 68 kPa (60 kPa on average). At each cycle of the recovery process, the water contact angle, contact angle hysteresis, and rolling off-angle were measured using a contact angle meter.

Results and discussion

Fig. 1 shows the overall process used to produce the superhydrophobic surface, which was synthesised by combining UHMWPE and PFOTES/TiO$_2$ NPs. UHMWPE was chosen because of its mechanical robustness, chemical stability and hydrophobicity. PFOTES/TiO$_2$ NPs were used for further reduction in surface energy of the composite and nanostructure formation. PFOTES/TiO$_2$ NPs were synthesised by the functionalization of hydrophilic TiO$_2$ using PFOTES (Fig. 1a). To synthesise the PFOTES/TiO$_2$ NPs, PFOTES and TiO$_2$ nanoparticles were mixed in a 99% ethanol solution and vortexed for 5 min. Then, the solution was coated on a glass substrate and dried in a dark room for 3 h. After that, PFOTES/TiO$_2$ NP powders were collected from the substrate. During the functionalization process, PFOTES molecules were covalently bonded to the TiO$_2$ surface (Note 1 & Fig. S2†). To characterise the bonding between PFOTES and TiO$_2$ NPs, X-ray photoelectron spectroscopy (XPS) analysis was employed. In the XPS overall survey, an F 1s peak at a binding energy of 689 eV was observed on TiO$_2$ NPs after the functionalization, indicating the presence of PFOTES on TiO$_2$ (Fig. 1b). In the O 1s XPS spectrum of intact TiO$_2$, three peaks at binding energies of 530.0, 532.0, and 533.4 eV were observed, corresponding to core oxygen, surface hydroxyls, and water adsorbates, respectively (Fig. 1c). After the PFOTES treatment, a new peak at a binding energy of 531.0 eV was observed, corresponding to Ti–O–Si, while the peak indicating hydroxyls reduced significantly (Fig. 1d).[32] The peak for Ti–O–Si was much lower than that of the oxygen core. This might be because the Si atomic percentage in the combination of PFOTES and TiO$_2$ NPs was very low, and it is estimated that in optimal conditions, <1% of total oxygen atoms interacted with PFOTES, creating Ti–O–Si bonding. As a result, the intensity of the binding energy indicating Ti–O–Si is relatively low compared to that of the oxygen core in the XPS analysis. Fourier transform infrared (FTIR) spectroscopy also confirmed the Ti–O–Si between 860 and 950 cm^{-1}, but the spectrum change was not significant, as shown in the XPS analysis.[33,34] In addition, CF$_2$ symmetric stretching was observed at 1146 cm^{-1}, indicating PFOTES on the functionalised TiO$_2$ NPs (Fig. S3†).[35]

The Ti–O–Si bonds formed between the terminal –OH of TiO$_2$ and C$_2$H$_5$O–Si of PFOTES resulted in the formation of the PFOTES/TiO$_2$ NPs (Fig. 1a). To produce a superhydrophobic surface, the PFOTES/TiO$_2$ NPs and UHMWPE powder were mixed. Then, 30 g of the resulting powder, which was loaded into a stainless-steel mould, was thermally compressed at ~11 MPa and 150 °C for 45 min, producing a smooth surface composite with a dimeter of ~6 cm and a thickness of ~1 cm (Fig. 1e). The composite samples were produced with various PFOTES/TiO$_2$ NP concentrations: PFOTES/TiO$_2$ NPs 30, 40, 50, and 60%. It was observed that with increasing PFOTES/TiO$_2$ NP concentrations, the sample became more hydrophobic but not superhydrophobic (Fig. S4†). To improve the hydrophobicity, the surface roughness of the samples was controlled through a sanding process using sandpapers including Grit no. 120, 240, 400, 800, and 1200 (Fig. S5†). The sand abrasion on the samples was conducted under a load pressure of 60 kPa on average. SEM and profilometer analysis showed that using sandpaper with a lower Grit number produced a rougher surface on the samples, and the roughness value increased up to ~17 μm (average of area roughness: S_a) (ESI Note 2, Fig. S6 and S7†).

3888 | *J. Mater. Chem. A*, 2024, **12**, 3886–3895

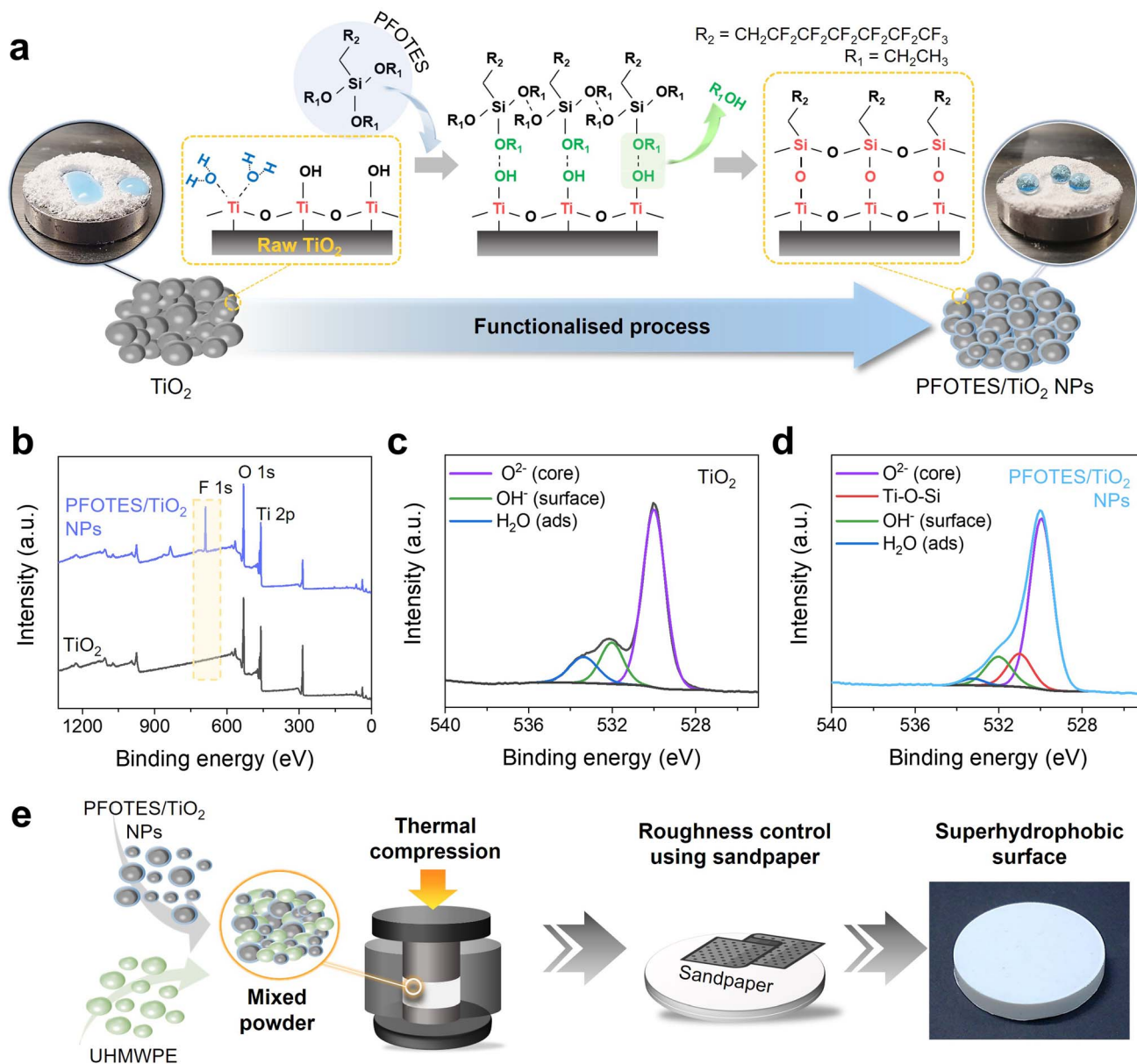This journal is © The Royal Society of Chemistry 2024

Fig. 1 Fabrication process of the superhydrophobic surface. (a) A schematic diagram illustrating surface functionalisation between TiO_2 and PFOTES. Insets show the hydrophilic TiO_2 (left) and hydrophobic PFOTES/TiO_2 NPs (right). (b) XPS overall survey of TiO_2 and PFOTES/TiO_2 NPs. (c and d) XPS O 1s scan of TiO_2 and PFOTES/TiO_2 NPs. The C 1s peak from adventitious carbon at 285.0 eV was used as an internal energy reference. (e) Schematic showing the fabrication process of the superhydrophobic surface.

Sandpaper abrasions enhanced the hydrophobicity of the surfaces, and the water contact angle of the samples increased with surface roughness (Fig. 2a). The water contact angle of pure UHMWPE linearly increased with surface roughness. Compared to UHMWPE, the contact angle of the composites containing PFOTES/TiO_2 NPs increased dramatically. The angle increment became steeper with an increase in the concentration of PFOTES/TiO_2 NPs in the composite. At an S_a of ~17 μm, pure UHMWPE gave a water contact angle of 154 ± 2.3°, while those of all composites containing PFOTES/TiO_2 NPs were ~160° (Fig. 2a).

Wenzel and Cassie–Baxter are the representative models to describe the wetting of surface roughness.[36,37] The Wenzel model is associated with a homogeneous regime in which liquid penetrates the grooves of rough surfaces, creating a sticky hydrophobic surface where water droplets stick to the surface.[38] In contrast, the Cassie–Baxter model is related to a heterogeneous regime in which air bubbles are entrapped in the groove, leading to a slippery superhydrophobic surface where water rolls even at low tip angles.[39] To understand the surface wettability of the samples, the Wenzel (1) and Cassie–Baxter (2) equations below were applied to the experimental data.[38–40]

$$\cos\theta_r = r\cos\theta_s \tag{1}$$

$$\cos\theta_r = f\cos\theta_s - (1 - f) \tag{2}$$

This journal is © The Royal Society of Chemistry 2024

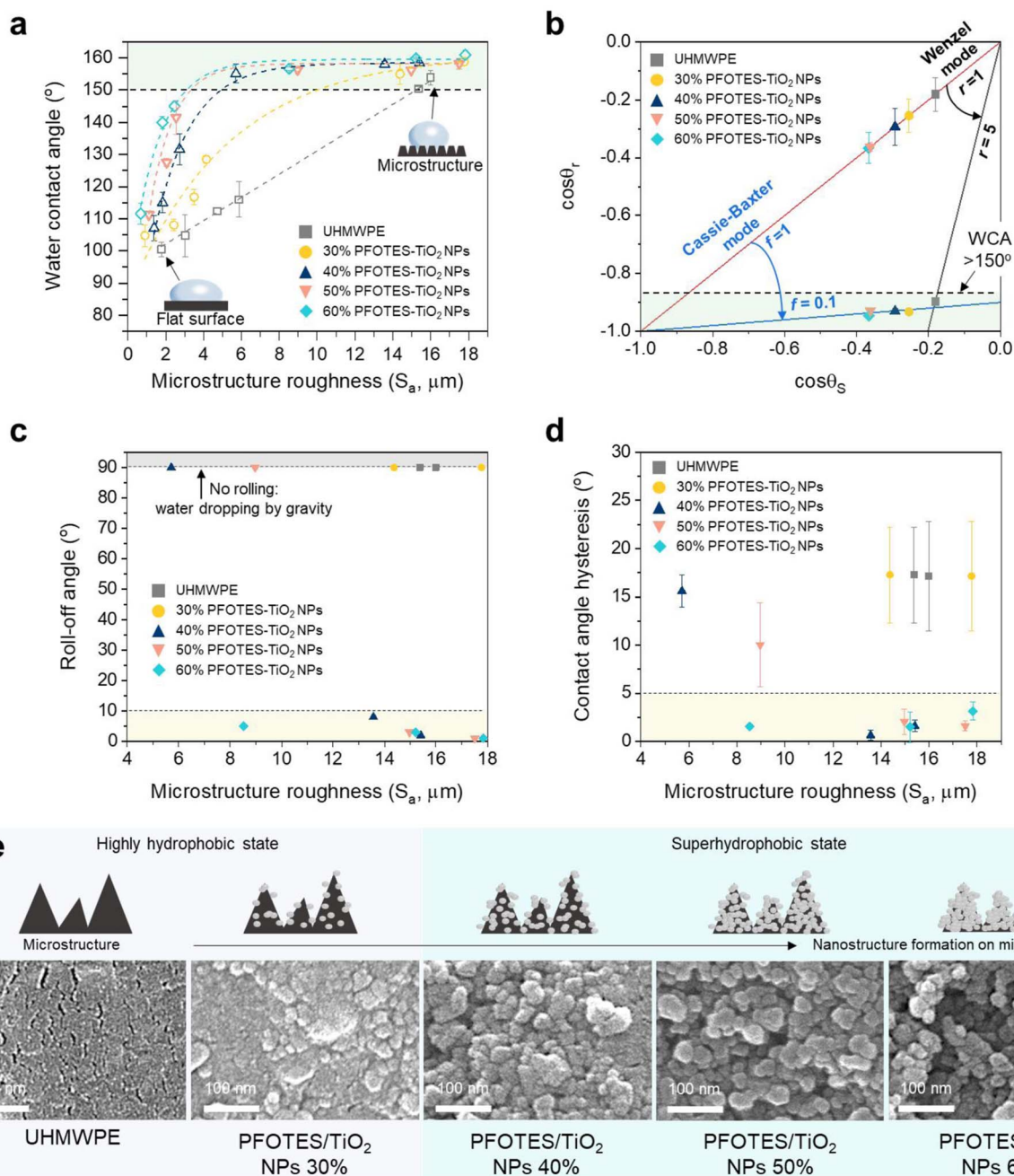J. Mater. Chem. A, 2024, 12, 3886–3895 | 3889

Fig. 2 Characterisations of superhydrophobic surfaces. (a) Change in the water contact angle of UHMWPE and composites with 30, 40, 50, and 60% PFOTES/TiO₂ NPs with increasing microstructure roughness. (b) Application of the Wenzel and Cassie–Baxter models to the water contact angles of UHMWPE and the composites. The red line indicates the Wenzel and Cassie–Baxter models when the roughness factor (r) and the fraction of the liquid/surface contact area (f) are 1, indicating a smooth surface. The blue line indicates the Cassie–Baxter model when f is ∼0.1, and the black line represents the Wenzel model when r is ∼5. (c and d) Water roll-off angle and contact angle hysteresis of UHMWPE and the composites with a water contact angle of >150°. (e) SEM images of nanostructure formation on microstructures of the UHMWPE and composites with 30, 40, 50 and 60% (the scale bar length = 100 nm). Data presented as mean ± standard deviation.

where θ_r and θ_s are the water contact angles on the rough and smooth surfaces, respectively, and r and f are the roughness factor and the fraction of liquid/solid surface contact interface, respectively.

The angle change of the pure UHMWPE sample by the increment of surface roughness complies with the Wenzel model, while the composites containing PFOTES/TiO₂ NPs are

well fitted to the Cassie–Baxter model (Fig. 2b, ESI Note 3, Fig. S8 and S9†). The model calculations showed that r was ∼5 when the UHMWPE sample in the Wenzel state had a water contact angle of 154 ± 2.3°. In the case of the composites in the Cassie–Baxter state, f values were ∼0.1 when the contact angles were ∼160°. In the measurements of contact angle hysteresis and rolling off-angle for the samples with the contact angles of

3890 | J. Mater. Chem. A, 2024, 12, 3886–3895

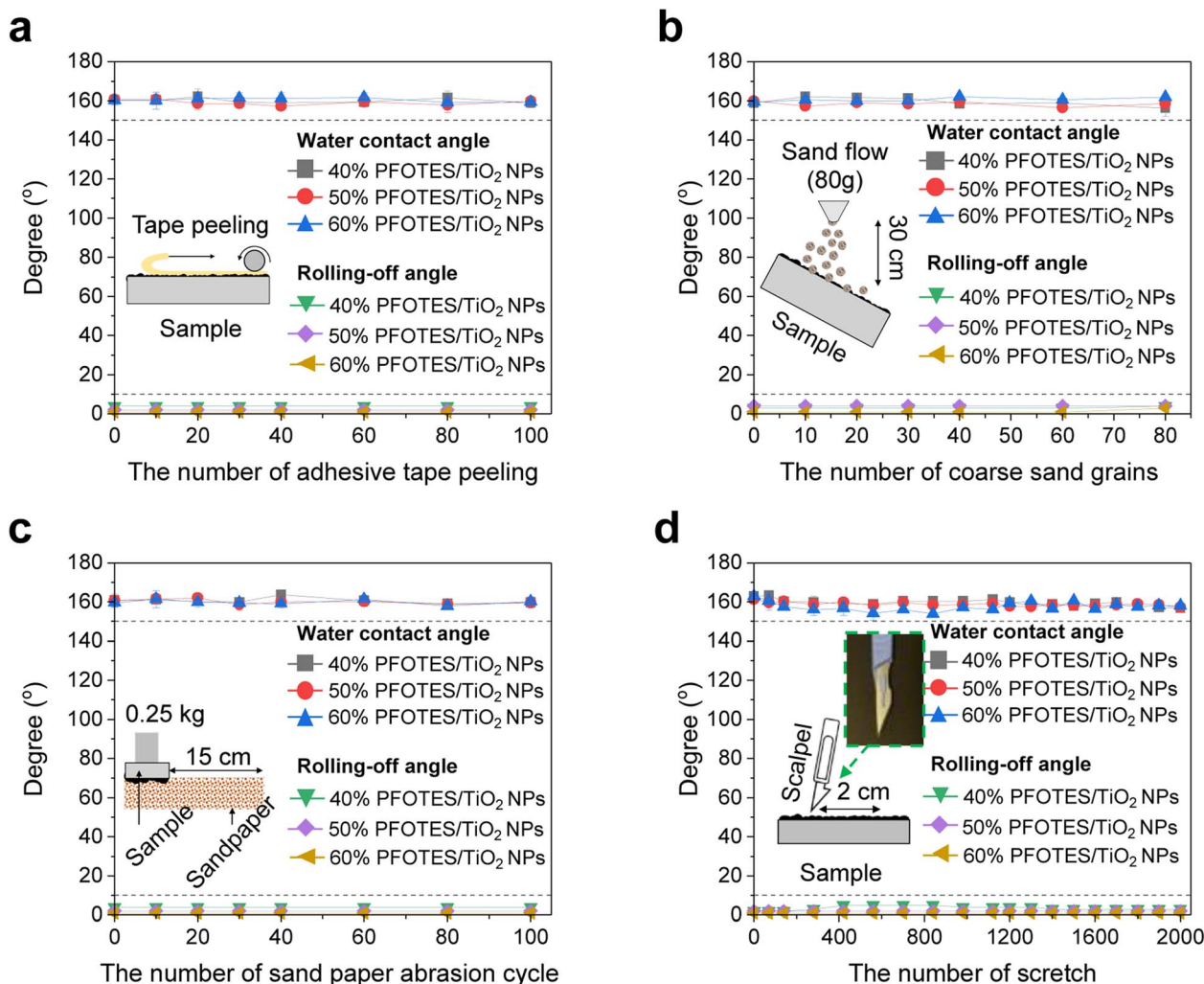This journal is © The Royal Society of Chemistry 2024

Fig. 3 Conventional robustness test of the superhydrophobic surface. Water contact angle and rolling off-angle after (a) adhesive tape peeling, (b) sand dropping, (c) sandpaper abrasion, and (d) scalpel scratch tests. Inset images show the schematic of the conventional stability test. Data presented as mean ± standard deviation.

>150°, water droplet rolling and low angle hysteresis were not observed on the pure UHMWPE and composite containing 30% PFOTES/TiO$_2$ NPs. Of the composites with ≥40% PFOTES/TiO$_2$ NPs, the samples with an S_a of >13 μm gave a low rolling off-angle (<10°) and contact angle hysteresis (<5°), indicating that they were superhydrophobic (Fig. 2c and d). In addition, the water dipping test showed that the composite containing ≥40% PFOTES/TiO$_2$ NPs only had a stable plastron effect shown from the superhydrophobic surface in the Cassie–Baxter state (ESI Note 3 and Fig. S10†).[12] Hydrophobic nano/microstructures on the surface are essential for superhydrophobicity as they minimise the interaction between water and the surface. SEM analysis of the samples with an S_a of >13 μm showed that the surface of the microstructures on the UHMWPE was relatively smooth compared to the composites (Fig. 2e). The addition of PFOTES/TiO$_2$ NPs into the UHMWPE caused the formation of nanostructures on the microstructures, and the structure size increased with increasing the NP concentration (Fig. 2e). The nanostructure was the most prominent at the highest concentration (60% PFOTES/TiO$_2$ NPs). The nanostructure formation is mainly attributed to the aggregated PFOTES/TiO$_2$ NPs in the composite. The sandpaper abrasions to produce the microstructures caused the aggregated nanoparticles to be excavated on the sample surface, and the increased addition of PFOTES/TiO$_2$ NPs into the composite resulted in greater nanostructure formation. The composite containing 30% PFOTES/TiO$_2$ NPs, which complied with the Cassie–Baxter model, showed a water contact angle of 158.8 ± 1.2° at an S_a of 17.7 ± 0.5 μm, but water contact hysteresis, rolling off-angle and plastron effect tests showed that it was not superhydrophobic.[25,41] This can be explained by assuming that the addition of 30% PFOTES/TiO$_2$ NPs was not sufficient to create hydrophobic nano/microstructures on the surface, suggesting that the sample was in the intermediate region between the Wenzel and Cassie–Baxter states.[42–44] Thus, it was concluded that 40–60% PFOTES/TiO$_2$ NPs in the composite were optimal for producing a superhydrophobic surface in the Cassie–Baxter state.

This journal is © The Royal Society of Chemistry 2024

J. Mater. Chem. A, 2024, 12, 3886–3895 | 3891

The composites containing 40, 50 and 60% PFOTES/TiO$_2$ NPs with an S_a of ~17 μm were selected as superhydrophobic surfaces. Water dropping and self-cleaning experiments against the selected samples showed that without surface wetting, water droplets were readily bound on and rolled off the samples tilted at angles of 5°–6°, and the water droplets rolling on the samples carried away dirt (ESI Videos S1 and S2†). Fig. 3 shows the conventional robustness test of superhydrophobic surfaces containing 40, 50, and 60% PFOTES/TiO$_2$ NPs. To determine the stability of the superhydrophobic surfaces, abrasion using Grit no. 80 sandpaper and coarse sand grain (1–2 mm in size) dropping, scalpel scratching, and adhesive tape peeling were employed. The experimental results showed that the surfaces gave a water contact angle of ~160° with a low contact angle hysteresis and rolling off-angle of <5° after 100 cycles of peeling, indicating the prolonged tape peeling-off did not affect the superhydrophobicity (Fig. 3a and S11a†). SEM images clearly showed that the adhesive tape peeling did not affect the nano/microstructures on the surfaces (Fig. S11b†). The coarse sand grain dropping test showed a similar result to the tape peeling test. The nano/microstructures and hydrophobicity were not affected by the 80-cycle sand dropping (Fig. 3b and S12†). After 100 cycles of sandpaper abrasion, quite minor wear on the surface was observed but the surface remained superhydrophobic (Fig. 3c and S13†). It showed that the wear under a load pressure of 250 g (6.1 kPa) did not damage the nano/microstructures because the nano/microstructures were produced through an abrasion process under a load pressure of 60 kPa on average. In addition, all superhydrophobic surfaces kept their water repellency even after scratching 2000 times, which is even exceptionally sharp (Fig. 3d). However, surface damage was observed on the superhydrophobic surfaces (Fig. S14†). The damage was clearly observed on the superhydrophobic surface with 60% PFOTES/TiO$_2$ NPs after 500 scratches, and in the case of the surface with 50% PFOTES/TiO$_2$ NPs, it was observed after 1000 scratches. The superhydrophobic surface with 40% PFOTES/TiO$_2$ NPs tolerated 2000 scratches, and the surface damage was minor. In addition, the superhydrophobic surfaces showed good stability against heat ranging from 20 to 180 °C and were highly repellent to water droplets with various pH levels (details in ESI Note 4 and Fig. S15 and S16†).

The mechanical strength of the superhydrophobic surfaces with 40, 50 and 60% PFOTES/TiO$_2$ NPs was determined using a universal testing machine and an iron ball with a weight of 265 g. Gypsum, white Portland (WP), grey Portland (GP), low-weight (LW), and high-strength (HS) cements were used as controls. The gypsum and cement samples were dried in a mould for 28 days to maximise the mechanical strength. Fig. 4 shows the tests of controls and superhydrophobic surfaces against compression, bending and impaction stress. The compressive strength of the superhydrophobic surface containing 60% PFOTES/TiO$_2$ NPs was higher than that of gypsum, WP, GP, and LP cement. However, it was slightly lower than that of HS cement fractured at a compressive stress of 38 ± 8.0 MPa. The compressive strength was enhanced by increasing the portion of UHMWPE within the surface. The hydrophobic

surface with 40 and 50% PFOTES/TiO$_2$ NPs had much higher compressive strength than the controls. In particular, the strength of the sample with 40% PFOTES/TiO$_2$ NPs was 1.7 times higher than that of HS cement (Fig. 4a).

A similar trend was also observed in bending strength (Fig. 4b). In the impact test using an iron ball, it was observed that the impact strength of all superhydrophobic surfaces was much higher than that of all controls. The hydrophobic surfaces were fractured at an impact energy of >180 kJ m^{-2}, while the controls were destroyed at <67 kJ m^{-2}, indicating that the
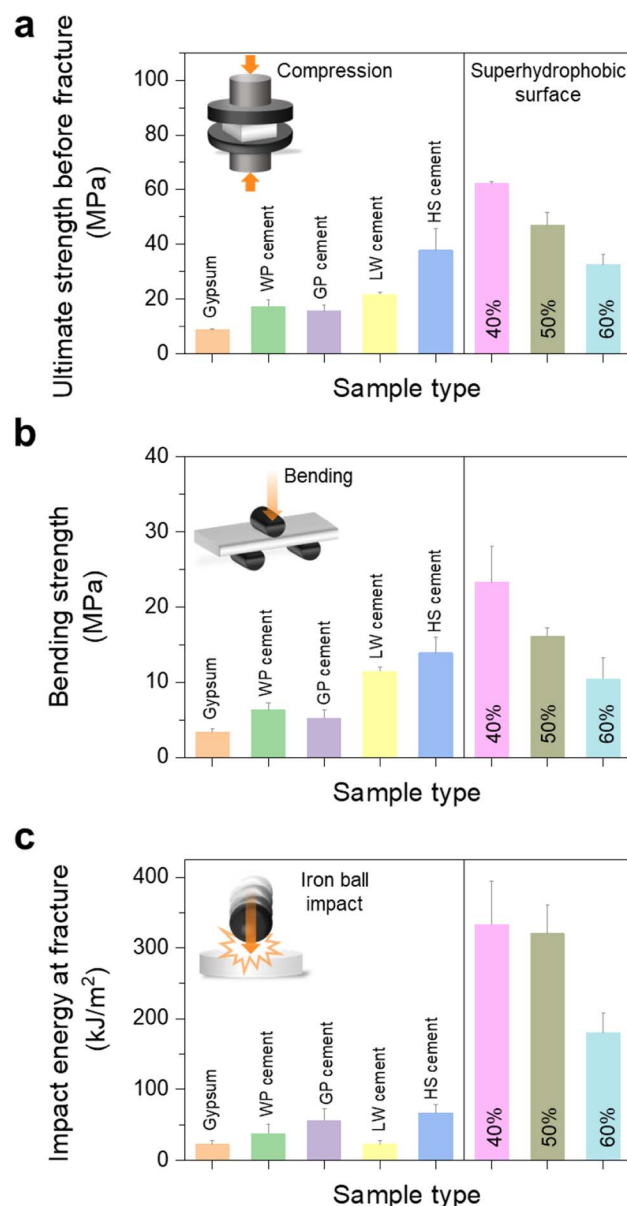

Fig. 4 Mechanical strengths of gypsum, WP, GP, LW, and HS cements and superhydrophobic surfaces containing 40, 50, and 60% PFOTES/TiO$_2$ NPs. (a) Compressive strength, (b) bending strength and (c) impact strength at the fracture point of the samples. Gypsum, white Portland (WP) cement, grey Portland (GP) cement, low-weight (LW) cement, and high-strength (HS) cement were used as controls. Data presented as mean $\pm$ standard deviation.

3892 | J. Mater. Chem. A, 2024, 12, 3886–3895

This journal is © The Royal Society of Chemistry 2024

superhydrophobic surfaces were 2.7–15 times stronger than the controls (Fig. 4c and ESI Video S3†). The superhydrophobic surfaces' mechanical robustness and resistance to various water pH levels and abrasion are mainly attributed to UHMWPE, accounting for 40–60% of the surfaces. The hydrophobic UHMWPE used in this study is mechanically robust and resistant to wear, acids, alkalis, and other chemical solvents.[45,46] The strong bonding between UHMWPE and PFOTES/TiO$_2$ NPs not only enhanced the mechanical strength and wear resistance but also the hydrophobicity of the surface, resulting in the production of highly robust superhydrophobic surfaces.

Fig. 5 shows the superhydrophobic recovery after surface damage and contamination under extreme conditions. The superhydrophobic surfaces were damaged through surface burning using a flame with a temperature of 2000 °C and aqua regia corrosion, resulting in a collapse of the nano/microstructures on the surfaces (Fig. S17†). The surface contact angles decreased to ~132°, indicating that they were hydrophobic. Grit no. 120 sandpaper abrasion at the length of 15 cm (a load pressure of 60 kPa on average) improved the water repellency of the damaged surfaces (Fig. 5 and S18†). The load pressure for the recovery was 10 times higher than that of the

abrasion test (Fig. S13†). After 10 or 50 abrasion cycles with sandpaper, all the samples gave a water contact angle of >150° with a rolling off-angle and contact angle hysteresis of <5° (Fig. 5a, b, S18a–d, ESI Videos S4 and S5†). The recovery trend of the surfaces contaminated by paint and oil was similar to that of the damaged surfaces. After the contamination, the contact angle decreased to ~108°. The 30 or 50-times cycled process successfully restored the superhydrophobicity of the surfaces (Fig. 5c, d, S18e–h, ESI Videos S6 and S7†). In addition, the surfaces contaminated by blood recovered their superhydrophobicity after 10 cycles of abrasion (ESI Note 5 and Fig. S19†). The results showed that the sanding process peels off the damaged or contaminated layer and creates hydrophobic nano/microstructures on the surface to make it superhydrophobic.

In the real world, superhydrophobic surfaces can lose hydrophobicity under various extreme conditions. For example, the nano/microstructures can be damaged and the surface fractured by an impact and friction with high-density materials, surface burn and corrosion, and surface contamination by impurities such as oil, paint and blood. Many techniques have been suggested to address the issues, but most research focused
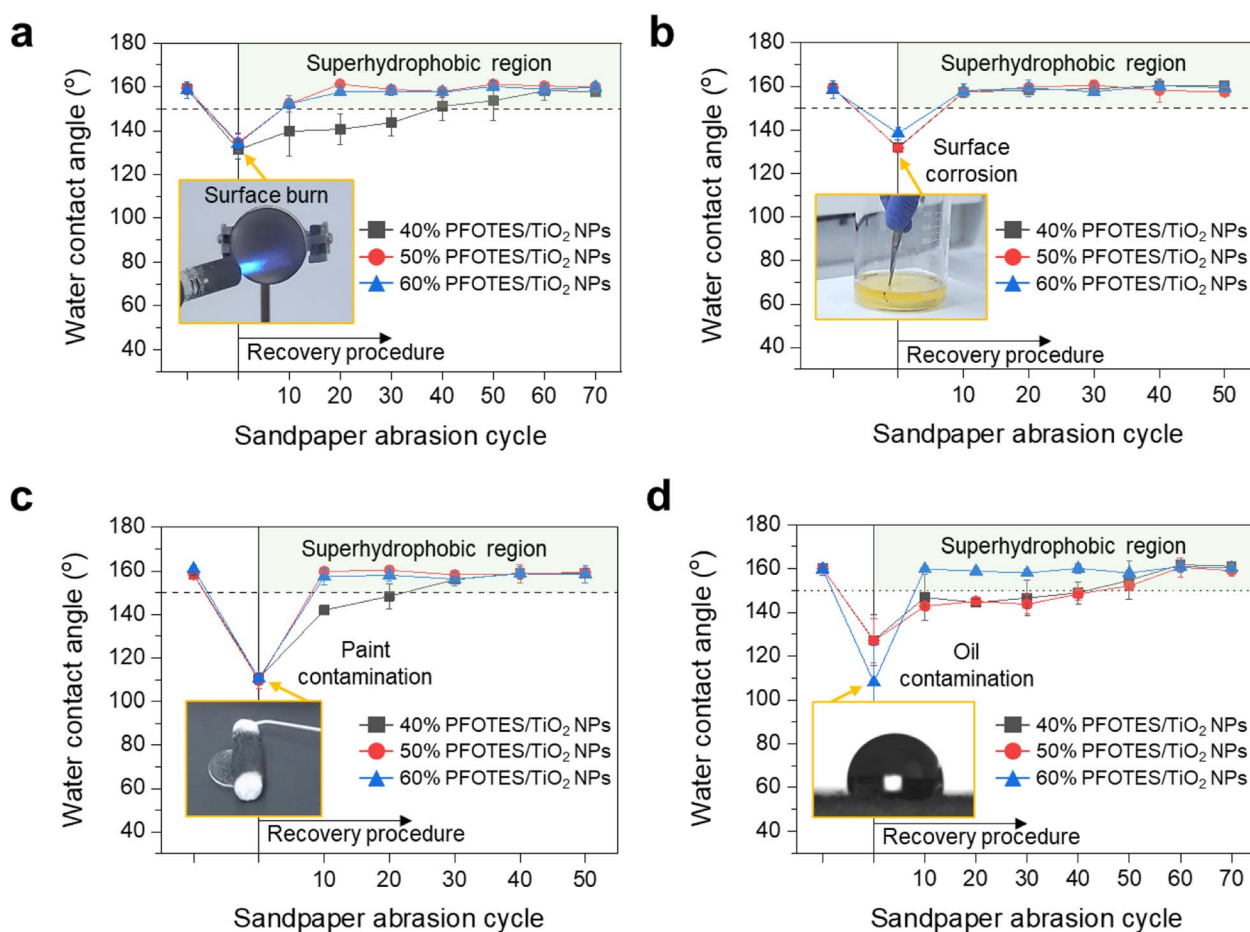

Fig. 5 Damage/contamination recovery of superhydrophobic surfaces containing 40, 50, and 60% PFOTES/TiO$_2$ NPs. (a) Surface burn by a flame with a temperature of 2000 °C. (b) Surface corrosion by aqua regia. (c and d) Paint and oil contaminations. Data presented as mean ± standard deviation.

This journal is © The Royal Society of Chemistry 2024

J. Mater. Chem. A, 2024, **12**, 3886–3895 | **3893**

on the wear-resistance superhydrophobic coating.[26–30] It was confirmed that the coating surfaces permanently lost super-hydrophobicity under extreme conditions, and it was impossible to recover the property (ESI Note 6 and Fig. S20†), indicating that to achieve superhydrophobicity, new multiple coating processes are necessary after removal of contaminated or damaged layers. Superhydrophobic surfaces with self-healing properties achieved *via* secretion of a low surface energy agent or from a regeneration process of the nano/microstructures have been reported. However, the surfaces are mechanically fragile and the healing properties were limited to wear or press damage only.[30]

Previous research introduced mechanically robust super-hydrophobic surfaces resistant to bending and compression stress. Zhang *et al.* (2017) showed a SiO$_2$/polymer-modified surface durable at a compressive strength of ~200 N,[47] Song *et al.* (2017) reported the surface, which consists of fluoroalkylsilane and concrete, with compressive and bending strengths of 9.1 and 3.9 MPa respectively,[48] and Liu *et al.* (2020) reported a robust surface, which consist of graphitic carbon nitride and polypropylene, with compressive and bending strengths of 27.1 and 6.0 MPa, respectively.[49] However, the mechanical strengths of these surfaces are lower than or similar to those of lightweight cement shown in Fig. 3a and b, and their surface damage resulted in a decrease of the water contact angle, indicating that the damage may cause a permanent loss of superhydrophobicity. Our study showed that the super-hydrophobic surface consisting of UHMWPE and PFOTES/TiO$_2$ NPs tolerated prolonged abrasion tests without losing their superhydrophobic property. It was repellent to water droplets with various pH levels and stable to thermal exposure at 180 °C. In particular, the surface's compressive (up to 62.2 MPa, equivalent to 5500 N) and bending strengths (up to 23.3 MPa) were more prominent than those of high-strength cement, which is widely known to be a robust material, or the surfaces in previous research.[47–49] Moreover, the damaged or contaminated surfaces recovered their superhydrophobicity through a simple sanding process, indicating that the robust surface can sustain the water-repellent properties under various extreme conditions and then recover.

Conclusion

This research shows that PFOTES/TiO$_2$ NP addition into UHMWPE changes the surface wettability from the Wenzel to Cassie–Baxter state, resulting in a mechanically robust super-hydrophobic surface recoverable from damage/contamination under extreme conditions. Contrary to other methods that required delicate techniques for the nano/microstructure formation, our research showed that the structures were formed through a simple abrasion process using sandpaper or a sanding machine, and the structure formation was not affected by the sanding abrasion direction (Fig. 2, S21, ESI Note 7 and Video S8†). In addition, various shaped and sized superhydrophobic surfaces were readily fabricated (ESI Video S9†).[26–30] The surfaces tolerated prolonged abrasion tests including sandpaper abrasion and coarse sand grain dropping, scalpel

scratching, and adhesive tape peeling without losing their superhydrophobicity, and their mechanical strengths were more prominent than those of high-strength cement, which is a highly robust material. Moreover, the damaged or contaminated surfaces recovered their superhydrophobicity through a simple sanding process, indicating that the robust surfaces can sustain the water repellent properties under various extreme conditions and then recover. This technique is expected to provide a tailored superhydrophobic surface for various applications, such as construction materials, water purification, drag reduction/buoyancy increase for a ship, electronic devices requiring water resistance, and irrigation systems.

Data availability

All data needed to evaluate the conclusions in the paper are present in the paper and/or the ESI.†

Author contributions

K. J. H. conducted most of the experiments and analysed the experimental results. J. H. Y. fabricated superhydrophobic surfaces. J. H. Y., W. H. and M. K. T. characterised the mechanical properties of the materials. J. S. conducted ATR-IR, XPS, and SEM analyses. J. H. J. advised and suggested the experiments. G. B. H. designed the experiments and supervised the research with advice from I. P. P. and C. J. C. G. B. H. and K. J. H. wrote the manuscript. G. B. H., I. P. P., and C. J. C. edited the manuscript.

Conflicts of interest

The authors declare that they have no competing interests.

Acknowledgements

References

1 J. Jeevahan, M. Chandrasekaran, G. Britto Joseph, R. B. Durairaj and G. Mageshwaran, *J. Coat. Technol. Res.*, 2018, **15**, 231–250.

2 X. Tian, T. Verho and R. H. Ras, *Science*, 2016, **352**, 142–143.

3 S. Pan, R. Guo, M. Bjornmalm, J. J. Richardson, L. Li, C. Peng, N. Bertleff-Zieschang, W. Xu, J. Jiang and F. Caruso, *Nat. Mater.*, 2018, **17**, 1040–1047.

3894 | *J. Mater. Chem. A*, 2024, **12**, 3886–3895

This journal is © The Royal Society of Chemistry 2024

4 X. Tang, P. Zhu, Y. Tian, X. Zhou, T. Kong and L. Wang, *Nat. Commun.*, 2017, **8**, 14831.

5 R. Blossey, *Nat. Mater.*, 2003, **2**, 301–306.

6 Y. A. Mehanna, E. Sadler, R. L. Upton, A. G. Kempchinsky, Y. Lu and C. R. Crick, *Chem. Soc. Rev.*, 2021, **50**, 6569–6612.

7 I. U. Vakarelski, N. A. Patankar, J. O. Marston and D. Y. Chan, *Nature*, 2012, **489**, 274–277.

8 F. Geyer, M. D'Acunzi, A. Sharifi-Aghili, A. Saal, N. Gao, A. Kaltbeitzel, T. F. Sloot, R. Berger, H. J. Butt and D. Vollmer, *Sci. Adv.*, 2020, **6**, eaaw9727.

9 Z. Li, A. Milionis, Y. Zheng, M. Yee, L. Codispoti, F. Tan, D. Poulikakos and C. H. Yap, *Nat. Commun.*, 2019, **10**, 5562.

10 G. B. Hwang, A. Patir, K. Page, Y. Lu, E. Allan and I. P. Parkin, *Nanoscale*, 2017, **9**, 7588–7594.

11 M. Liu, S. Wang and L. Jiang, *Nat. Rev. Mater.*, 2017, **2**, 17036.

12 Z. Guo, W. Liu and B. L. Su, *J. Colloid Interface Sci.*, 2011, **353**, 335–355.

13 Y. Liu, L. Moevius, X. Xu, T. Qian, J. M. Yeomans and Z. Wang, *Nat. Phys.*, 2014, **10**, 515–519.

14 H. Y. Erbil, A. L. Demirel, Y. Avci and O. Mert, *Science*, 2003, **299**, 1377–1380.

15 A. Dhyani, J. Wang, A. K. Halvey, B. Macdonald, G. Mehta and A. Tuteja, *Science*, 2021, **373**, 294.

16 A. Gauthier, S. Symon, C. Clanet and D. Quere, *Nat. Commun.*, 2015, **6**, 8001.

17 N. R. Chiou, C. Lu, J. Guan, L. J. Lee and A. J. Epstein, *Nat. Nanotechnol.*, 2007, **2**, 354–357.

18 M. Sbragaglia, A. M. Peters, C. Pirat, B. M. Borkent, R. G. Lammertink, M. Wessling and D. Lohse, *Phys. Rev. Lett.*, 2007, **99**, 156001.

19 S. Herminghaus, *Europhys. Lett.*, 2007, **52**, 165.

20 K. J. Kubiak, M. C. T. Wilson, T. G. Mathia and P. Carval, *Wear*, 2011, **271**, 523–528.

21 C. Li, J. Zhang, J. Han and B. Yao, *Sci. Rep.*, 2021, **11**, 459.

22 A. Patir, G. B. Hwang, C. Lourenco, S. P. Nair, C. J. Carmalt and I. P. Parkin, *ACS Appl. Mater. Interfaces*, 2021, **13**, 5478–5485.

23 T. S. Wong, S. H. Kang, S. K. Tang, E. J. Smythe, B. D. Hatton, A. Grinthal and J. Aizenberg, *Nature*, 2011, **477**, 443–447.

24 A. K. Epstein, T. S. Wong, R. A. Belisle, E. M. Boggs and J. Aizenberg, *Proc. Natl. Acad. Sci. U.S.A.*, 2012, **109**, 13182–13187.

25 G. B. Hwang, K. Page, A. Patir, S. P. Nair, E. Allan and I. P. Parkin, *ACS Nano*, 2018, **12**, 6050–6058.

26 W. Zhang, D. Wang, Z. Sun, J. Song and X. Deng, *Chem. Soc. Rev.*, 2021, **50**, 4031–4061.

27 Y. Lu, S. Sathasivam, J. Song, C. R. Crick, C. J. Carmalt and I. P. Parkin, *Science*, 2015, **347**, 1132–1135.

28 C. Peng, Z. Chen and M. K. Tiwari, *Nat. Mater.*, 2018, **17**, 355–360.

29 D. Wang, Q. Sun, M. J. Hokkanen, C. Zhang, F. Y. Lin and Q. Liu, *Nature*, 2020, **582**, 55–59.

30 S. Y. Xiang and W. D. Liu, *Adv. Mater. Interfaces*, 2021, **8**, 2100247.

31 T. Huhtamäki, X. Tian, J. T. Korhonen and R. H. A. Ras, *Nat. Protoc.*, 2018, **13**, 1521–1538.

32 J. Abad, C. Gonzalez, P. L. de Andres and E. Roman, *Phys. Rev. B: Condens. Matter Mater. Phys.*, 2010, **82**, 165420.

33 D. Kannaiyan, S. T. Kochuveedu, Y. H. Jang, Y. J. Jang, J. Y. Lee, J. Lee, J. Kim and D. H. Kim, *Polymers*, 2010, **2**, 490–504.

34 T. Song, P. Zhang, T. Wang, A. Ali and H. Zeng, *Nanoscale*, 2018, **10**, 2275–2284.

35 R. H. Brody, H. G. Edwards and A. M. Pollard, Fourier transform-Raman spectroscopic study of natural resins of archaeological interest, *Biopolymers*, 2002, **67**, 129–141.

36 A. Lafuma and D. Quere, *Nat. Mater.*, 2003, **2**, 457–460.

37 M. Marmur, *Langmuir*, 2003, **19**, 8343–8348.

38 R. N. Wenzel, *Ind. Eng. Chem.*, 1936, **28**, 988–994.

39 A. B. D. Cassie and S. Baxter, *Trans. Faraday Soc.*, 1944, **40**, 546–551.

40 T. Onda, S. Shibuichi, N. Satoh and K. Tsujii, *Langmuir*, 1996, **12**, 2125–2127.

41 I. A. Larmour, S. E. Bell and G. C. Saunders, *Angew. Chem.*, 2007, **46**, 1710–1712.

42 D. M. Lopes, S. M. M. Ramos, L. R. de Oliveira and J. C. M. Mombach, *RSC Adv.*, 2013, **3**, 24530–24534.

43 K. Madry and W. Nowicki, *Eur. Phys. J. E*, 2021, **44**, 138.

44 G. Nagayama and D. Zhang, *Soft Matter*, 2020, **16**, 3514–3521.

45 S. Kurtz, *The UHMWPE Handbook*, Academic Press, 1st edn, 2004.

46 J. Tong, Y. Ma, R. D. Arnell and L. Ren, *Composites, Part A*, 2006, **37**, 38–45.

47 X. Zhang, D. Zhi, L. Sun, Y. Zhao, M. K. Tiwari, C. J. Carmalt, I. P. Parkin and Y. Lu, *J. Mater. Chem. A*, 2018, **6**, 357–362.

48 J. Song, D. Zhao, Z. Han, W. Xu, Y. Lu, X. Liu and B. Liu, *Chem. Eng. J.*, 2020, **385**, 123969.

49 S. Liu, W. Wan, X. Zhang, A. D. Crema and S. Seeger, *J. Mater. Chem. A*, 2017, **5**, 14545–14550.

This journal is © The Royal Society of Chemistry 2024

J. Mater. Chem. A, 2024, **12**, 3886–3895 | **3895**